Scientia Iranica C (2022) 29(6), 3151–3165

Sharif University of Technology
Scientia Iranica
Transactions C: Chemistry and Chemical Engineering
http://scientiairanica.sharif.edu

A theoretical kinetic and classical dynamic investigation of CN+OH and CN+OD reactions on an interpolated potential energy surface

A. Sabah and Sh. Ramazani*

Department of Chemistry, Yasouj University, 7493475918 Yasouj, Iran.

Received 25 November 2021; received in revised form 8 March 2022; accepted 9 May 2022

KEYWORDS
Cyano radical;
Reaction dynamics;
Reactive cross section;
Reaction probability;
Scattering angle.

Abstract. In the current work, kinetic and dynamic parameters in reactive and non-reactive collisions between CN and OH radicals were investigated upon an interpolated potential energy surface using MP2/6-311G++(d,p) ab-initio method. The total and individual reaction probabilities and cross-sections for all reactions were obtained and applied to calculate the rate constant and rate expression. In non-reactive trajectories, the effect of the impact parameter and relative translational energy of particles on the deflection angle was also studied. To investigate the kinetic isotopic effect, the deuterium was used instead of hydrogen atom to illustrate the effect of mass of attacking radical and target molecules on physical observables including reaction probability and cross-section.

1. Introduction

Despite the significant deal of effort made in recent years to clean up the environment, pollution remains the main problem and poses continuing risks to human health. These problems are undoubtedly the largest in the developing world, where traditional sources of pollution like industrial emissions, poor sanitation, inadequate waste management, and contaminated water supplies consumed by a large number of human beings, even in developed countries, are affected by air pollution produced from biomass fuels, although environmental pollution is supposed to exert the highest impact on the poor sections of society [1,2]. Because of severe environmental contamination caused by the ignition of nitrogenous compounds, the dynamics of these compounds in combustion have been the subject of intense experimental and theoretical research.

The empty space between stars is full of particles such as H_2, NH, OH, HNO, CO, and CN. Despite the simplicity of the structure of these molecules, the issue of chemical understanding and physical conditions of these particles in Interstellar Medium (ISM) remains to be solved. The temperature ranges of ISM are very extensive, from 10 K (cold temperature) to 106 K (high temperature). Many of these particles are combustion systems that have attracted much attention by astrophysics as a subfield of combustion. Therefore, combustion systems are very important all around the world.

Therefore, the presence of reactive radicals and different particles in the combustion and atmosphere processes gives rise to the complexity of their chemistry [3–6].

It is important to note that chemical kinetic calculations play an important role in obtaining information about the combustion process in chemistry. Moreover, these types of calculations are critical to predicting astrochemical models. From a

*. *Corresponding author.*
E-mail address: ramazani@yu.ac.ir (Sh. Ramazani)

doi: 10.24200/sci.2022.59394.6226

chemical point of view, various factors such as rate constant and the effect of quantum numbers on the primary and final states are important for a clear understanding of the collision [7,8]. However, the study of the chemistry of nitrogen molecules in the interstellar environment is very important.

Nowadays, there is a great deal of interest in reducing NO_X emissions from combustion sources like fixed power generation stations. Therefore, to perform this reduction, many strategies such as combustion modification, re-burn technologies, and selective non-catalytic reduction of NO (SNCR processes) have been suggested [9]. In order to chemically remove NO_X in the SNCR technologies, three main SNCR strategies can be used: thermal De-NO_X process (NH_3), RAPRENO$_X$ process $(HOCN)_3$, and NO_XOUT process $(NH)_2CO$, all of which are implemented with the addition of different species to the post combustion gases. The important point is that in these cases, a deeper understanding of the reactions leading to NO_X reduction is not complete [10].

For production of NO_X in the combustion systems, three main mechanisms have been reported up to now. The first is the Zeldovich mechanism, which started at high temperatures by the $O(^3P)$+N_2 reaction. The second is the Fennimore or prompt NO_X mechanism, initiated from the reaction between N_2 gas and simple radicals like CH and CH_2, and fuel fixed nitrogen sources, started with the HCN oxidation [9]. Moreover, the last mechanism to produce NO_X involves many reactions and chemical reagents. Therefore, for this reason, it is much more complex and has been more difficult to explain [11]. The gas-phase reactions including cyano radical, $CN(X^2\Sigma^+)$, happen in different media like flames, gas lasers, and planetary atmospheres [12–14].

One of the most significant species in the chemistry of both NO_X generation and reduction processes is CN radical. As pointed earlier, the CN radical is obtained directly by the Fenimore mechanism [9] and fuel-fixed nitrogen oxidation chemistry; therefore, it plays a significant role in the chemistry of SNCR. Up to now, the High-Temperature Shock Tube (HTST) investigation carried out by Wooldridge et al. [15] is only the direct empirical results of this reaction.

Moreover, one of the first radicals detected in cometary comae is the CN radical and it has one of the strongest spectral signatures after OH. The cyano radical was shown in 1P/Halley for the first time, thus illustrating the possibility of original gas in cometary comae environment [16]. However, the source of the CN radical in comets is still not completely clear and there are multiple potential parent species.

The results demonstrate that there are many significant rate-controlling reactions happening in the second-stage ignition regime, where the total conversion of HCN into N_2 occurs via primary reactions with OH and H [15]. To investigate the chemistry of CN radical, the CN+OH reaction is an important reaction. This reaction could produce different types of products including a terminating reaction, leading to the reduction of the pool of radicals. This can cause NCO or NH regents for reduction or production of NO_X [15]. Therefore, the HCN reactions lead to CN production, followed by a fast radical-radical reaction:

$$CN + OH \rightarrow \text{Products}.$$

The ground-state reaction of the titled reaction (cyano radical, $CN(X^2\Sigma)$) with the hydroxyl radical, $OH(^2\Pi)$, has five exothermic product channels shown in Box I, where $\Delta H_f^0(0)$'s, in kJ.mol^{-1}, of these species are taken as follows: CN = 432 ± 4 [17], OH = 36.9 ± 0.4 [18], HNC = 195.4 ± 4.2 [19], $NH(\alpha^1\Delta) = 508.3 \pm 1.3$ [20], $NH(X^3\Sigma) = 356.9 \pm 1.3$ [21], NCO = 129.5 ± 2.5 [17].

So far, only two studies have been reported on the kinetics of CN+OH reaction.

First, in 1996, Wooldridge et al. [15] used the narrow-line laser absorption measurements to determine the rate constant for CN + OH → Products in the nominal temperature range of 1000–1900 K. The values of rate constants that the researchers reported for titled reaction are in the range of $4-5\times10^{-13}$ cm^3.mol^{-1}.s^{-1}.

The rate constant for the reaction of the cyano radical, $CN(X^2\Sigma)$, with the hydroxyl radical,

$$\begin{aligned}
CN(X^2\Sigma) + OH(X^2\Pi) &\rightarrow HCN(X^1\Sigma) + O(^3P); && \Delta H_f^0(0) = -26.5 \pm 10.4 \text{ kJ.mol}^{-1},\\
&\rightarrow NH(\alpha^1\Delta) + CO(X^1\Sigma); && \Delta H_f^0(0) = -74.4 \pm 1.3 \text{ kJ.mol}^{-1}\\
&\rightarrow HCN(X^1\Sigma) + O(^3P); && \Delta H_f^0(0) = -88.7 \pm 6.2 \text{ kJ.mol}^{-1},\\
&\rightarrow NCO(X^1\Pi) + H(^3S); && \Delta H_f^0(0) = -129.5 \pm 6.5 \text{ kJ.mol}^{-1},\\
&\rightarrow NH(X^3\Sigma) + CO(X^1\Sigma); && \Delta H_f^0(0) = -225.8 \pm 1.3 \text{ kJ.mol}^{-1}.
\end{aligned}$$

Box I

OH($X^2\Pi$), has been measured to be $(1.4 \pm 0.48) \times 10^{-10}$ cm^3.molecule^{-1}.s^{-1} at a temperature of 292±2 K by Decker et al. [22].

The main objectives of the current work are the kinetics investigation of CN+OH reaction and calculation of the probability of reaction and rate coefficient. Hydrogen is also a substitute for the heavier isotope (deuterium) to understand the effect of the mass of attacker and target species on the observable properties (reaction probability, cross-section, and rate constant). At the end of this manuscript, the importance of rotationally inelastic collisions for those systems is examined.

$$\mathrm{CN + OH} \longrightarrow \text{Products} \quad (R1)$$
$$\longrightarrow \mathrm{CNOH} \quad (R2)$$
$$\longrightarrow \mathrm{HON + C} \quad (R3)$$
$$\longrightarrow \mathrm{ONC + H} \quad (R4)$$
$$\longrightarrow \mathrm{HOCN} \quad (R5)$$
$$\longrightarrow \mathrm{HOC + N} \quad (R6)$$
$$\longrightarrow \mathrm{OCN + H} \quad (R7)$$
$$\longrightarrow \mathrm{OCNH} \quad (R8)$$
$$\longrightarrow \mathrm{CNH + O} \quad (R9)$$
$$\longrightarrow \mathrm{CO + NH} \quad (R10)$$
$$\mathrm{CN + OD} \longrightarrow \text{Products} \quad (R11)$$
$$\longrightarrow \mathrm{CNOD} \quad (R12)$$
$$\longrightarrow \mathrm{DON + C} \quad (R13)$$
$$\longrightarrow \mathrm{ONC + D} \quad (R14)$$
$$\longrightarrow \mathrm{DOCN} \quad (R15)$$
$$\longrightarrow \mathrm{DOC + N} \quad (R16)$$
$$\longrightarrow \mathrm{OCN + D} \quad (R17)$$
$$\longrightarrow \mathrm{OCND} \quad (R18)$$
$$\longrightarrow \mathrm{CND + O} \quad (R19)$$
$$\longrightarrow \mathrm{CO + ND} \quad (R20)$$

2. Method

2.1. Computational details

In this research, the electronic structure calculations were carried out using GAUSSIAN 03 package [23]. All stable species and transition states on the PES were optimized by using second-order Møller-Plesset perturbation theory (MP2) level of theory with a 6-311++G(d,p) standard basis set. Calculations of harmonic vibrational frequencies of the relaxed configurations are performed using the same method for correction of energies of molecules being necessary for kinetic calculations. Frequencies were also used to determine the saddle points from local minima. In the MP2/6-311++G(d,p) optimized geometries, single-point energy calculations at the CCSD(T)/6-311++G(d,p) levels of theory were carried out.

Figure 1 shows the values for the bond length (in angstrom) and angles (degree) of some configurations including the reactants, products, intermediates, and transition state structures at the MP2/6-311++G(d, p) level of ab-initio calculations.

The relative energies of the stationary points placed on the potential energy surface of the reaction CN+OH at the CCSD(T)/6-311++G(d,p) levels of theory are shown in Figure 2. As shown in this figure, there are several reactive channels depending on the orientation of the species.

The collision between cyano radical and OH radical leads to two intermediates including HOCN and HONC. If the OH radical comes close to the carbon side of CN, HOCN molecule is produced. The HOCN form is converted into OCNH through TS1. This intermediate via two different channels is changed into HOC+N and OCN+H with relative energies of 447.8 and -1209.8 kJ.mol^{-1}, respectively. These steps are performed without any barrier. Another intermediate (HONC) can be formed from the reactants directly. Moreover, the HONC intermediate through two different channels is changed to HON+C and ONC+H with relative energies of 652.2 and 138.0 kJ.mol^{-1}, respectively. These steps are performed without any barrier.

The HOCN intermediate is 248.2 kJ.mol^{-1} more stable than other intermediates. As presented in Figure 2, some products including HOC+N, HON+C, ONC+H, OC+NH, and O+CNH have higher relative energies than other species on the potential energy surface justifying their low production. The minimum stationary point of this potential energy surface is 1200 kJ.mol^{-1} under CN+OH.

As was reported in Table 1, relative energies of stationary points at the level of CCSD(T) are compared with this value at the MP2 level of theory. Of note, all values were modified with zero-point energies.

2.2. Form of the potential energy surface

Construction of a potential energy surface for a reactive or nonreactive chemical reaction is an important issue in molecular dynamics. The nature of the PES can

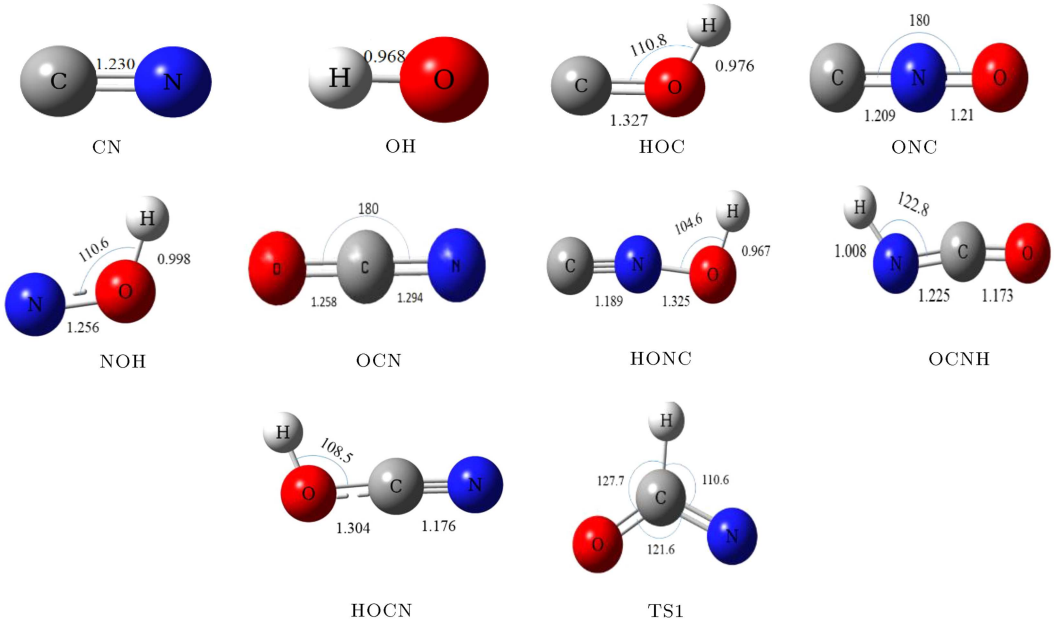

Figure 1. Optimized structures of the stationary points at the MP2/6-311++G** level. Angles are in degrees and bond lengths are in angstroms.

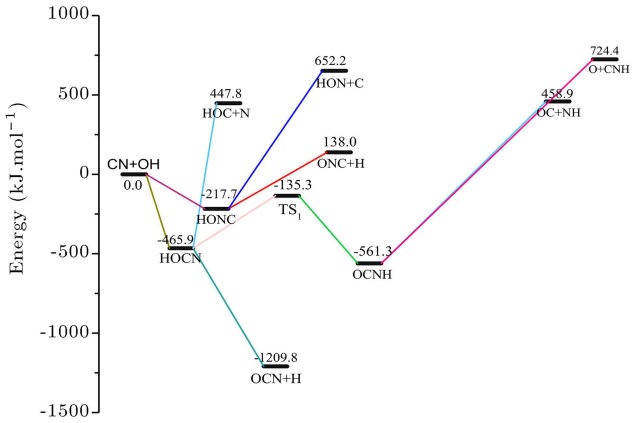

Figure 2. Relative energies of stationary points at the CCSD (T)/6-311++G**//MP2/6-311++G** level of theory in kJ.mol^{-1}. All values were corrected with zero-point energies.

Table 1. Relative energies of all products at different levels of theory (kJ.mol^{-1}).

R	CCSD(T)	MP2	ZPE
OH+CN	0.00	0.00	30.89
HOCN	-465.92	-628.87	55.77
HOC+N	447.82	385.76	35.95
OCN+H	-1209.81	-380.29	20.80
TS1	-135.31	-225.63	46.80
OCNH	-561.30	-730.27	56.77
ONC+H	138.04	-376.70	24.40
HONC	-217.75	-358.73	55.49
HON+C	652.23	608.02	37.67

be formed either experimentally or through theoretical calculations [24–27].

In the current work, the modified Shepard interpolation method over a set of data points of ab initio calculation was applied to construct the PES using Grow methodology. This method was explained elsewhere completely [24,28]; therefore, only a brief description of it is given here. For reactions of up to four atoms, we can utilize all the bond lengths as internal coordinates.

Therefore, here, we will be considering a PES for a four-atom system, in particular the CN+OH reaction. As demonstrated in Schematic 1, the PES for titled reaction is formed utilizing the six interatomic distances, $R = \{R_1, R_2, R_3, R_4, R_5, R_6\}$.

The potential energy of a data point, R, in the vicinity of a reference data point, $R(i)$, can be expanded as a Taylor expansion, T_i, at these interatomic distances. However, a more physically reasonable asymptotic behavior is achieved when this Taylor expansion is expressed in inverse length coordinates, Z, rather than interatomic distances (where $Z \equiv 1/R_n$):

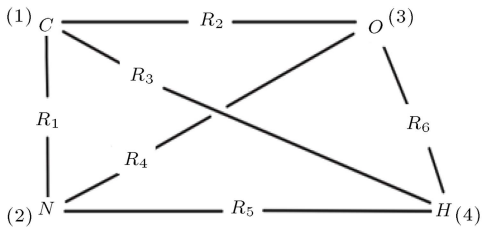

Schematic 1. Representation of all internal coordinates.

$$T_i(Z) = V[Z(i)] + \sum_{k=1}^{3N-6} [Z_k - Z_k(i)] \left.\frac{\partial V}{\partial Z_k}\right|_{Z=Z(i)} + \frac{1}{2!} \sum_{k=1}^{3N-6} \sum_{j=1}^{3N-6} [Z_j - Z_j(i)] \times [Z_j - Z_j(i)] \left.\frac{\partial^2 V}{\partial Z_k \partial Z_j}\right|_{Z=Z(i)} + \cdots, \quad (1)$$

where $V[Z(i)]$ is potential energy at $Z(i)$, and the derivatives are taken with respect to inverse distances at $Z(i)$. Here, the Taylor expansions are truncated to second order. The utility of higher-order expansions has already been investigated [29].

A modified Shepard interpolation method [30,31] gives the value of total potential energy at any configuration, R, as a weighted average of the Taylor series about all starting data points, N_d, and their symmetry equivalents.

$$V(R) = \sum_{g \in G} \sum_{i=1}^{N} w_{g=1}(R) T_{g=i}(Z), \quad (2)$$

where:

$$w_i(R) = \frac{v_i(R)}{\sum_{g \in G} \sum_{k=1}^{N_d} v_{g_k^0}(R)}. \quad (3)$$

The normalized weight function, w_i, weights the contribution of the Taylor expansion about each of $R(i)$ data points to the total potential energy at configuration R. Data points "spatially close" to R will have higher weights than those at high distances. This is obtained by utilizing the un-normalized weight function, v_i:

$$v_i(R) = \frac{1}{\|R - R(i)\|^{2p}}. \quad (4)$$

$v(R)$ converges to the exact potential in the limit $N_d \to \infty$ when the power p is sufficiently large ($p = 9 - 12$).

The weight function in Eq. (2) changes faster close to $Z(i)$ than that for the Potential Energy Surface (PES) to be an interpolation of the data at $Z(i)$ which made unphysically sharp features in the PES. This problem was solved using the following equation:

$$v_i = \left\{ \left[\sum_{n=1}^{\frac{N(N-1)}{2}} \left(\frac{Z_n - Z_n(i)}{d_n(i)} \right) \right]^{\frac{q}{2}} + \left[\sum_{n=1}^{\frac{N(N-1)}{2}} \left(\frac{Z_n - Z_n(i)}{d_n(i)} \right) \right]^{\frac{p}{2}} \right\}, \quad (5)$$

$$d_n(i)^{-6} = \frac{1}{M} \sum_{j=1}^{M} \frac{\left\{ \left[\left.\frac{\partial E}{\partial Z_n}\right|_{Z(j)} - \left.\frac{\partial T_i}{\partial Z_n}\right|_{Z(j)} \right] [Z_n(j) - Z_n(i)] \right\}^2}{E_{tol}^2 \|Z(j) - Z(i)\|^6}, \quad (6)$$

where $p > 3N - 3$ and $q > 2$, but $q << p$. In Eq. (5), $d_n(i)$ is defined as a confidence length.

3. Results

3.1. Classical dynamics calculation

In this paper, calculations of reaction cross-sections, reaction probability, and scattering angle via the classical dynamic simulations and construction of PES were carried out. The PES was evaluated through interpolation of some initial ab-initio data points. To study the trajectories, the velocity-Verlet integration algorithm was employed at a time step of 1.0×10^{-17}s, the starting value of impact parameter of 0, and the initial center of mass distance separation from the CN radical to the OH fragment of 5.0 Bohr.

The maximum impact parameter $b_{\max}$ is 4.0 Bohr compared with $r_{CN} + r_{OH}$, which is about 3.97 Bohr. The reactant radicals were given random orientation, zero rotational angular momentum, and vibrational energies in accordance to their ZPVE level. To create a microcanonical distribution of initial atomic positions and velocities for the classical trajectories, a Markov walk was applied. The number of Markov chain steps per trajectory and Markov step length for all fragments were set at 500 and 0.15 Å, respectively.

The relative translational energies between the reactant's fragments ranged between 9.19–23.63 kJ.mol^{-1} which corresponded to $T = 1105.30 - 2842.05$ K. A total of 2400 data points were produced from interpolation of 110 initial points. The final PES was interpolated over a batch of 2400 points.

Finally, a set of 1500 trajectories for the reactions between reactants were run at several sizes of the interpolation data set in order to determine the stability and convergence of the reaction probability due to the size of the data set. Next, these batches of 1500 trajectories were applied for the final data set of 2400 points in order to determine the physical observable properties such as reaction probability, cross sections, and rate constant for reactive collisions.

The distribution of the energy values for the data points is depicted with a histogram in Figure 3 at MP2/6-311++G(d,p).

The maximum area of the curve (−200 to −570 kJ.mol^{-1}) corresponds approximately to the energies of the HOCN, HONC, and OCNH, which are intermediate on this potential energy surface. A

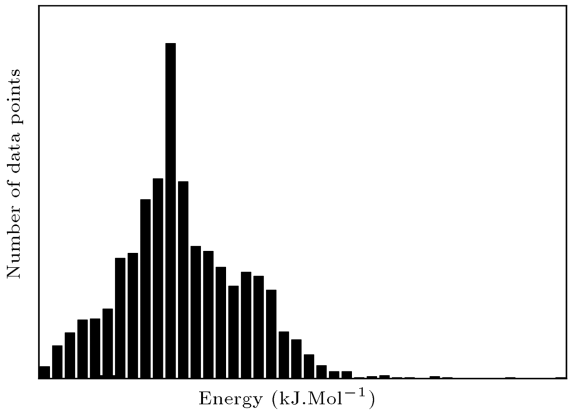

Figure 3. The distribution of the 2400 data points. The energy of every point was given relative to the energy of reactants.

comparison between Figures 2 and 3 shows that the most stable configurations are OCNH and OCN+H. Moreover, the number of data points with energy higher than the reactant molecules is small; therefore, these molecules are kinetically less likely to be produced.

The best way to test the convergence of the interpolation is the stability of calculated observable parameters such as reaction probability or cross-sections from the PES. The alteration of the probability of reaction for CN+OH with the PES data set size is given in Figure 4.

As shown in this figure with the addition of the points to the PES data set, the probability of reaction does not change significantly; therefore, the data point in the POT file is enough to calculate the dynamics of reaction. This result is in accordance with our previous study on H+HCN and NH+OH reactions [6,32,33].

The reaction probability as a function of impact

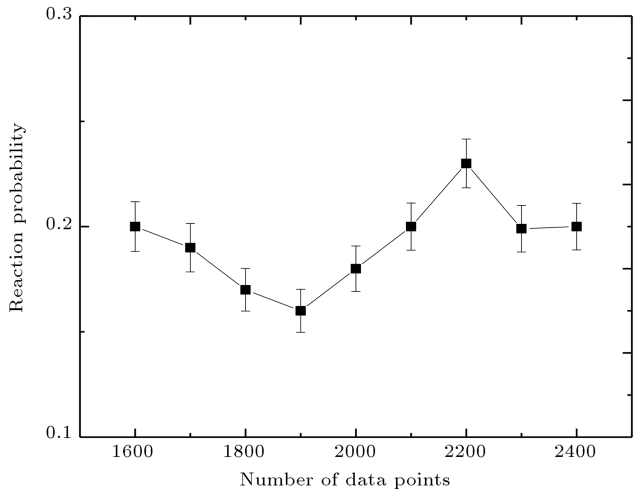

Figure 4. The calculated reaction probability with respect to the number of date point.

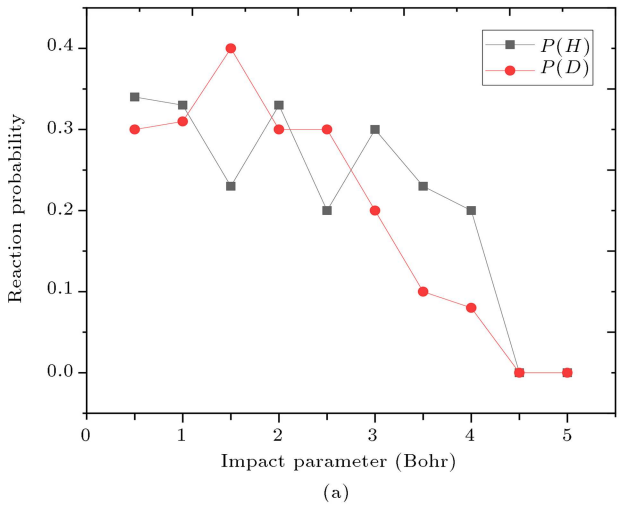

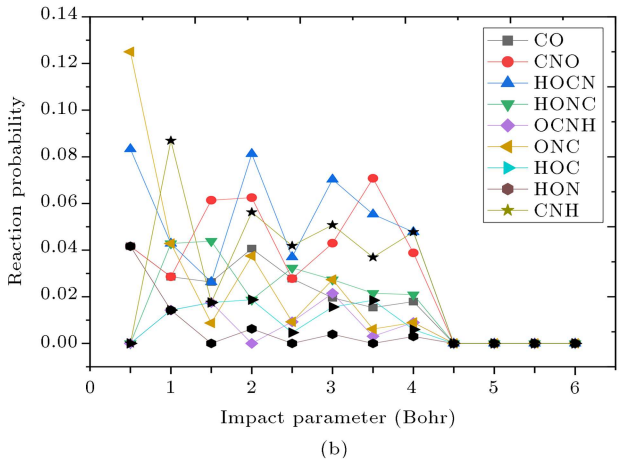

Figure 5. (a) Reaction probability as a function of impact parameter with a relative translation energy of 23.62 kJ.mol^{-1}. (b) The reaction probability plotted as a function of impact parameter for $R2$ to $R10$ reactions at 23.69 kJ.mol^{-1}.

parameter from 1500 trajectories, in which the relative kinetic energy is 23.62 kJ.mol^{-1}, is plotted in Figure 5(a). This parameter was calculated for R1 and R11 as the main reactions in this article.

According to Figure 5(a) and (b), the reaction rates of channels and reaction probability of products depend on the mass of fragment particles and the energy path of each trajectory. As indicated in Figure 5(a), upon increasing the value of impact parameter, the reaction probability converged to small values (close to zero). Figure 5(a) shows that fragments would not interact at interval distance more than 4.5 Bohr such that no reaction occurred and there were only non-reactive collisions.

To perform the reaction, the impact parameter should be small enough for OH and OD to hit the CN effectively. This is more evident for the lighter particle (H) than the heavier one (D). The reaction between CN and OH ($R1$, including light atom (H)) has a higher

reaction probability than the reaction between CN and OD ($R11$, including heavy atom (D)).

The effect of reaction probability on impact parameter at various energies is illustrated in Figure 6 for $R1$ reaction at three different relative translation energies. As seen in this figure and Figure 7, as the relative translational energy (or temperature) increases, the probability of reaction increases, too.

Because of the increasing number of collisions between OH and OD with CN at a higher translational energy, the probability of reaction increased. The relative kinetic energy of the fragments ranged from 9.19 to 23.63 kJ.mol^{-1}.

Figure 8 shows the total cross-section for hydrogen and its isotopic exchange with respect to energy in the collection of 1500 trajectories and several relative translational energies over a range of 9.19 to 23.63 kJ.mol^{-1}. Cross-section similar to the reaction probability increased as the translational energy increased.

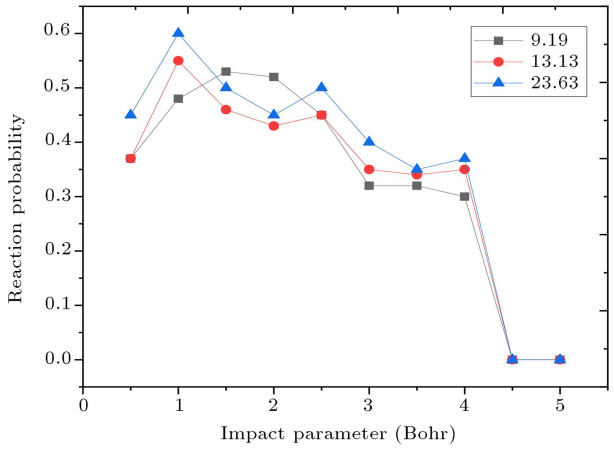

Figure 6. Reaction probability represented as a function of impact parameter for $R1$ reaction at 9.19, 13.13, and 23.62 kJ.mol^{-1} relative translation energies.

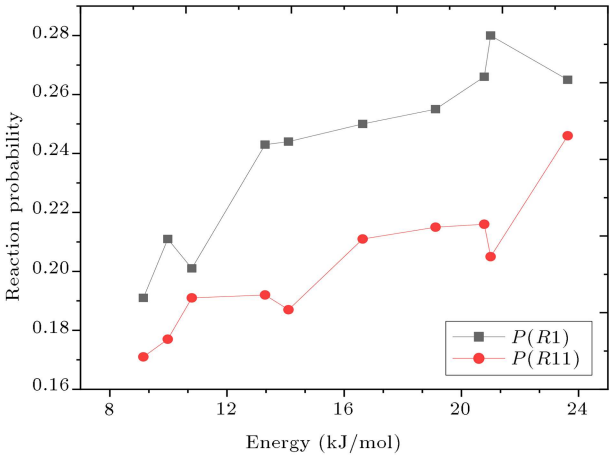

Figure 7. The total reactive reaction probability as a function of relative translation energy.

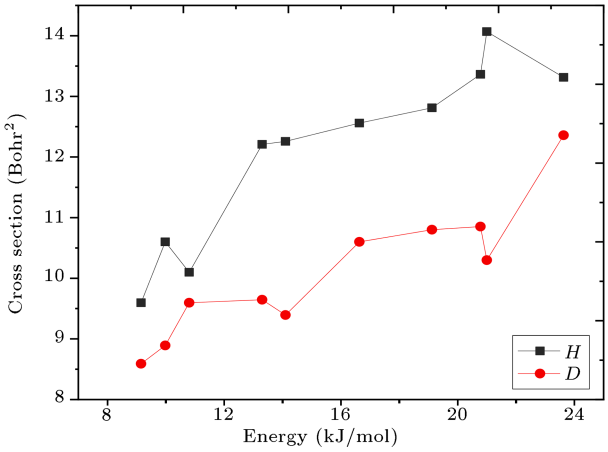

Figure 8. The total reaction cross-section as a function of relative translation energy.

3.2. *Mass effects on observables data of main reactions*

It was noticed that the reactions rate and reaction probability depended on the mass of particles and the translation energy of the molecules [34]. In the current part, some of reactions and their deuterated analogs were selected to study the effects of mass of target molecule and incident molecule on the kinetic and dynamic of reaction [35]. $R11$ reaction represents the reactions where hydrogen of reactant was substituted by deuterium. Here, ($R2$)–($R12$) and ($R7$)–($R17$) reactions were the subsets of ($R1$) and ($R11$), respectively. The results of classical dynamics simulations indicate that because of different masses of incident molecules (OH and OD), there were differences in the kinetics data such as reaction probability, cross-section, and rate coefficient (Figure 8).

The comparison of the reaction probability is shown below in which HOCN and ONC are the original products in Channels 1 and 2, respectively.

$$P_{r,\mathrm{HOCN}} > P_{r,\mathrm{OCN}} > P_{r,\mathrm{CNH}} > P_{r,\mathrm{HONC}} > P_{r,\mathrm{NH}} > P_{r,\mathrm{ONC}} > P_{r,\mathrm{HOC}} > P_{r,\mathrm{OCNH}} > P_{r,\mathrm{HON}},$$

and:

$$P_{r,\mathrm{ONC}} > P_{r,\mathrm{DOCN}} > P_{r,\mathrm{DOC}} > P_{r,\mathrm{DON}} > P_{r,\mathrm{DONC}} > P_{r,\mathrm{ND}} > P_{r,\mathrm{OCND}} > P_{r,\mathrm{CND}} > P_{r,\mathrm{OCN}}.$$

As shown earlier, the process of comparing reaction probability in channel one (hydrogen branch) differs from that in channel two (deuterium branch); this indicates the effect of mass on the reaction rate. For this purpose, we compare the reactions ($R1 - R10$) with reactions ($R11 - R20$), respectively. As reported in Figure 5(b) and Table 2, HOCN, HOC, OCN, and CNH are the main products in channel one and DOCN and DOC are the main products in channel two.

Table 2. The ratio of the reaction probability of reactions of branch one (H transfer) to $R1$ and branch two (D transfer) to $R11$.

E (kJ.mol^{-1})	$P_2/P_1(P_{12}/P_{11})$	$P_3/P_1(P_{13}/P_{11})$	$P_4/P_1(P_{14}/P_{11})$
9.15	0.068 (0.041)	0.058 (0.088)	0.026 (0.047)
9.98	0.069 (0.045)	0.069 (0.051)	0.042 (0.068)
10.80	0.060 (0.063)	0.050 (0.099)	0.040 (0.034)
13.30	0.042 (0.064)	0.046 (0.068)	0.063 (0.057)
14.10	0.086 (0.048)	0.049 (0.080)	0.038 (0.040)
16.63	0.079 (0.069)	0.044 (0.055)	0.040 (0.062)
19.12	0.077 (0.040)	0.046 (0.098)	0.042 (0.030)
19.95	0.068 (0.054)	0.090 (0.089)	0.036 (0.047)
21.00	0.086 (0.051)	0.048 (0.083)	0.057 (0.033)
23.63	0.087 (0.083)	0.066 (0.074)	0.062 (0.043)
E (kJ.mol^{-1})	$P_5/P_1(P_{15}/P_{11})$	$P_6/P_1(P_{16}/P_{11})$	$P_7/P_1(P_{17}/P_{11})$
9.15	0.179 (0.147)	0.211 (0.259)	0.221 (0.194)
9.98	0.176 (0.220)	0.152 (0.203)	0.194 (0.169)
10.80	0.189 (0.146)	0.129 (0.234)	0.229 (0.208)
13.30	0.228 (0.167)	0.188 (0.194)	0.208 (0.190)
14.10	0.169 (0.160)	0.189 (0.214)	0.235 (0.187)
16.63	0.163 (0.118)	0.190 (0.241)	0.198 (0.189)
19.12	0.192 (0.150)	0.165 (0.250)	0.173 (0.185)
19.95	0.158 (0.155)	0.203 (0.209)	0.173 (0.206)
21.00	0.188 (0.127)	0.143 (0.210)	0.191 (0.188)
23.63	0.217 (0.185)	0.196 (0.166)	0.168 (0.200)
E (kJ.mol^{-1})	$P_8/P_1(P_{18}/P_{11})$	$P_9/P_1(P_{19}/P_{11})$	$P_{10}/P_1(P_{20}/P_{11})$
9.15	0.021 (0.018)	0.189 (0.153)	0.037 (0.059)
9.98	0.023 (0.012)	0.203 (0.175)	0.069 (0.051)
10.80	0.015 (0.023)	0.224 (0.125)	0.065 (0.063)
13.30	0.021 (0.027)	0.208 (0.174)	0.054 (0.057)
14.10	0.022 (0.016)	0.144 (0.176)	0.058 (0.079)
16.63	0.016 (0.027)	0.187 (0.163)	0.056 (0.069)
19.12	0.038 (0.028)	0.158 (0.150)	0.065 (0.050)
19.95	0.023 (0.020)	0.162 (0.163)	0.083 (0.054)
21.00	0.040 (0.037)	0.170 (0.220)	0.075 (0.044)
23.63	0.028 (0.034)	0.101 (0.143)	0.077 (0.074)

Figure 8 also presents the variation of cross-section as a function of relative translation energy of reactants that exhibited a similar behavior as reaction probability. As expected, the cross-section and reaction probability increase with an increase in the temperature in all reactions.

3.3. Inelastic scattering calculations

Having information about the rotationally and vibrationally inelastic collisions is very significant for understanding energy transfer between molecules and atoms. When the scattering is not elastic (new particles are produced), the energy and direction of the scattered atoms are independent variables, unlike the elastic scattering situation. As drawn in Figure 5, the maximum reactive reaction probability, even in the case of low-impact parameters, is less than 0.34, implying about 70% of the trajectories. Therefore, it is important to study the non-reactive reaction and inelastic scattering calculations. In inelastic collisions, some of the inner energies of CN and OH radicals are exchanged between the particles or are coupled into translation energy. If

the collision between the incident or lighter particle (OH), whose kinetic energy is T, and the target or heavier molecule (CN) is head-on, the distance of the closest approach D can be calculated by equating the starting kinetic energy to the Coulomb energy in the closest approach, i.e.:

$$T = \frac{zZe^2}{4\pi\varepsilon_\circ D}, \tag{7}$$

or:

$$D = \frac{zZe^2}{4\pi\varepsilon_\circ T}, \tag{8}$$

at which point the α-particle would come back completely, i.e., the scattering angle θ would be equal to π. In other words, when the line of OH radical is distance b from the CN particle, then the scattering angle will be smaller. The b and θ are related to each other through the following equation [36]:

$$\tan\left(\frac{\theta}{2}\right) = \left(\frac{D}{2b}\right). \tag{9}$$

This equation is derived from Newton's Second Law of Motion, Coulomb's law for the force between the OH and CN particles, and conservation of angular momentum. Of note, if $\theta = \pi$, then $b = 0$ as mentioned above. When b increases, OH particle partially collides with CN radical, thus decreasing the scattering angle. For CN$\cdots$OH collision, the long-range potential is smooth such that no generalization can be made about the interaction area. In this research, the behavior of the scattering angles with the impact parameters differed from the ones mentioned above in the case of low-impact parameters.

In the current work, the alteration of scattering angle at different energies with respect to impact parameter was studied. As shown in Figure 9, at non-reactive trajectories, refracted particles were found in the scattering angle range of 0.4 to 1.15°. This angle is dependent on the energy of the particles and decreases following an increase in energy. It is clear that in the case of small-impact parameters, the scattering angle of CN radical indirectly depends on the impact parameter and relative translational energy, while at higher b, this dependence is weaker. The graph shows that the variation of scattering angle with an approximation includes three impact parameter zones for 16.5 kJ.mol^{-1} as translational energy:

i. Lower than 6;
ii. Between 6 and 9;
iii. Larger than 10.

In the case of other energies, there are also three areas, the size of which varies only. At distances less than d_{AB} ($d_{AB} = 1/2(d_{\mathrm{OH}} + d_{\mathrm{NH}})$, calculated by ab-initio calculations, the value of scattering angle is reduced greatly upon increase in the value of the impact parameter.

In this section, there is a reverse relationship between the impact parameter and the scattering angle. In case of a head-on collision, the scattering function was the same as a hard-sphere collision. In a region where $b > d_{AB}$, the scattering angle is not very sensitive to the variation of impact parameter. At distances between 6 and 9, there is an inverse relationship between scattering angle and impact parameter, which is derived from the difference orientation of OH and NH in the same impact parameter. When two molecules belonging to electric spheres approach each other with different orientations, they collide with different sizes and their scattering angle varies. At 23.62 kJ.mol^{-1}, out of 1500 trajectories in total, there were 235 trajectories with $6 < b < 9$. At some of these trajectories, particles with the same b were aggregated at different orientations and were scattered at various angles.

In conclusion, small separation distance ($6 < b < 9$) happened between two molecules, leading to different interactions and therefore different scattering angles. For this reason, this study reports the average of scattering angle for every b. Considering some energies of this region (6 to 9) and in the case of impact parameter value being more than 9, the curve shows that variation of impact parameter does not affect the scattering angle and then, the curve becomes flat. In addition, at larger b ($b > 10$) values, there were trajectories with no collision. Therefore, there was a weaker affinity between the scattering angle and impact parameter, making these particles hardly scattered given that the attractive part of the Lennard-Jones potential rapidly fell to zero in this area. Another important point to gain from this figure is that upon

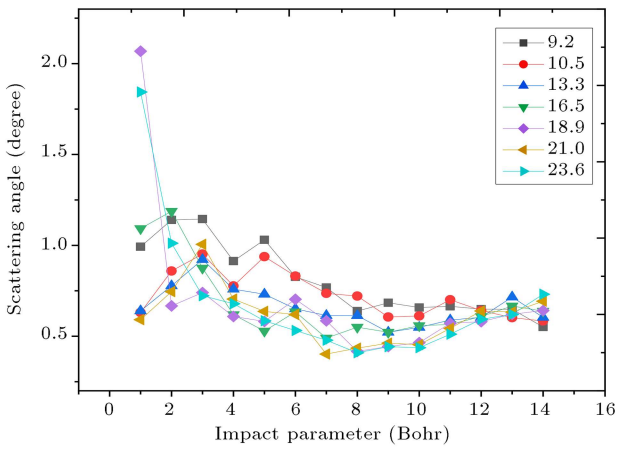

Figure 9. Scattering angle as a function of impact parameter for non-reactive $R1$ reaction.

Table 3. Scattering angle expressions at different relative translational energies.

E (kJ.mol^{-1})	$b < d_{OH-CN}$	$b > d_{OH-CN}$
9.15	$\theta = 5.6390 - 2.9961b$ $(1 \leq b < 4)$	$\theta = 14.7563 - 11.0460b$ $(8 < b < 12)$
10.80	$\theta = 1.4224 - 3.1520b$ $(1 \leq b < 7)$	$\theta = 0.7595 - 23.1529b$ $(8 < b < 14)$
13.30	$\theta = 5.2477 - 2.3402b$ $(1 < b < 6)$	$\theta = 5.5382 - 8.0659b$ $(8 < b < 10)$
16.63	$\theta = 9.4120 - 6.9805b$ $(1 < b < 7)$	$\theta = 0.0195 - 19.5323b$ $(11 < b < 13)$
19.12	$\theta = 6.2030 - 2.5899b$ $(1 < b < 7)$	$\theta = 5.6390 - 2.9961b$ $(8 < b < 12)$
21.00	$\theta = 7.9709 - 5.9070b$ $(1 < b < 7)$	$\theta = 0.0579 - 19.8493b$ $(8 < b < 14)$
23.63	$\theta = 7.1758 - 3.9887b$ $(1 < b < 7)$	$\theta = 1.5560 - 17.6491b$ $(8 < b < 14)$

increasing the amount of energy, the scattering angle converges faster and better to zero at large b. For this relation, it was observed that a fitting was used to evaluate the scattering angle expressions, as reported in Table 3. If the OH radical with various relative translation energies come close to the CN particle at a constant b, the dispersed molecules would be found at different scattering angles.

As mentioned earlier, the scattering angle is dependent on the impact parameter. Moreover, it depends on relative energy at a constant impact parameter. In addition, mean dispersed particles with special energy are seen at a particular diffraction angle. The impact parameter and relative energy are two important factors that have many different effects on the scattering angle values. Scattering angle as a function of relative energy in several impact parameters is drawn in Figure 10. Depending on the relative kinetic energy of reactant molecules, the variation of energy is of different impact on θ. With increase in the values of impact parameters, the nonreactive reaction probability is reduced. From the investigation of angular momentum in different impact parameters, it can be concluded that energy is transferred between two reactants. Although the CN particle was irrotational, it was found after non-reactive collisions that CN molecule obtained energy, rotationally excited.

As illustrated in Figure 11, as the impact parameter increased in value, the average rotational angular

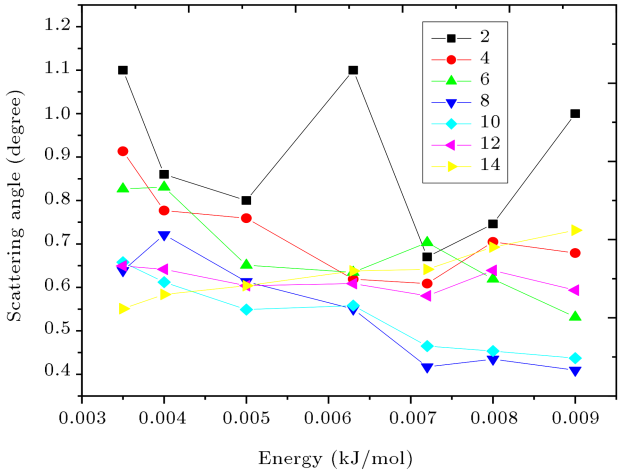

Figure 10. Scattering angle plotted as a function of relative translational energy for non-reactive $R1$ reaction.

momentum for the products of nonreactive collisions was reduced. Such a trend was also observed in previous studies [6]. As seen in this figure, because of the collision between particles even at $b > 16$ Bohr, the final average angular momentum of CN remains nonzero. However, these collisions are nonreactive and the energy is transmitted solely between two reactant molecules.

The obtained cross-sections for angular momentum transfer to the initially irrotational CN and OH particles with respect to size of data point are given

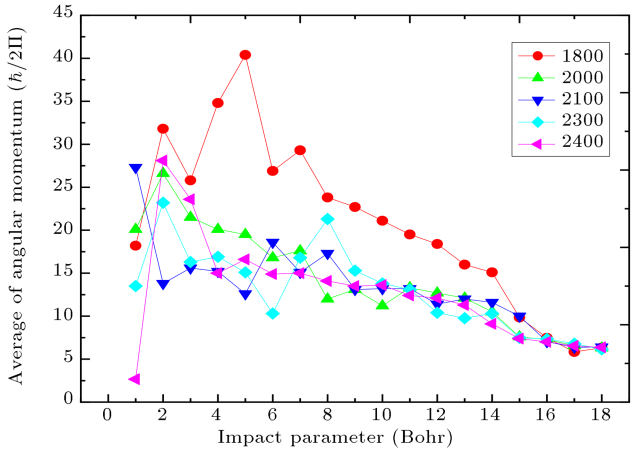

Figure 11. The final average angular momentum of CN in nonreactive collisions shown as a function of the impact parameter. The initial translational energy was 23.63 kJ.mol^{-1}.

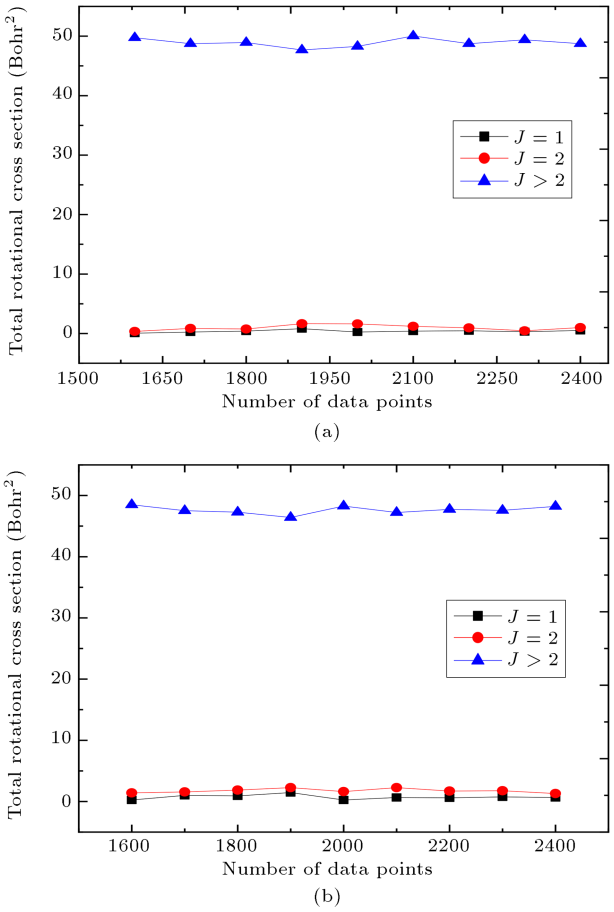

Figure 12. Total rotationally inelastic cross-sections reported with respect to the data set size at a different value of J(CN). The initial relative translational energies were 23.63 kJ.mol^{-1}.

in Figure 12. Initial relative translational energy is 23.63 kJ.mol^{-1}. The classical final angular momentum was converted into J level and binned into integer J levels for obtaining cross-sections. In CN and OH species and in the final $J = 1$, $J = 2$, and $J > 2$, the obtained cross-sections converged to a constant number when the numbers of data points increased. As expected, the non-reactive cross-sections in Figure 12 exceed those in reactive collisions, as illustrated in Figure 8.

3.4. Rate coefficient calculations

The reaction cross-section σ_R and the reaction probability can be calculated from the classical mechanics. According to the collision theory and physically reasonable assumptions, a simple expression for the rate coefficient can be written as a function of reaction cross-section $\sigma(E)$ at temperature T. Therefore, the relationship among the quantities of rate constant $k(T)$, cross-section σ_R, and the probability of reaction P and different approaches to the description of the nuclear dynamics are given below:

$$k(T) = \left[\frac{8}{\pi\mu(k_B T)^3}\right]^{\frac{1}{2}} \int_0^{\infty} E\sigma(E)\exp(-E/k_B T)dE, \tag{10}$$

where μ is the reduced mass of reactants and k_B is Boltzmann's constant. $\sigma(E)$ is the reactive cross-section ($\pi(b^2_{\max})P_r$) and $P_r = N/N_r$, where N and N_r are the total number of all trajectories and the number of trajectories leading to the product, respectively. The reaction cross-sections are also expressed as a power law: $\sigma(E) = AE^{\gamma}$ (with $\gamma > -2$).

The calculated total reactive cross-section is given in Figure 8, jointly with the data of fitting based on $\sigma(E) = AE^{\gamma}$. The total QCT reactive cross-section illustrated in Figure 8 for the MP2 surface could be approximately fitted to the following expression in unit of Å^2. After integration, the integral is easily solved to obtain the rate constant:

$$k(T) = a\left[\frac{8}{\pi\mu}\right]^{\frac{1}{2}} \Gamma(\gamma+2)(k_B T)^{\gamma+1/2}, \tag{11}$$

in which $\Gamma(x)$ is the Gamma function.

The fitting parameters (including a and γ) calculated from non-linear least square method for R_{1-10} to R_{11-20} reactions are reported in Table 4.

These parameters were employed to calculate the total reactive cross-section. Finally, the fitted rate coefficient expressions were calculated. The rate expressions combine two parts: pre-temperature factor and temperature-dependent parts. To investigate the impact of temperature on the calculated rate coefficient, the Arrhenius plot as a function of temperature is drawn in Figure 13. As indicated in this figure, increase in temperature (or relative translational energy of reactants) increases the value of calculated rate constant.

As shown in the reaction schematic in the introduction section, reactions in the current work are

Table 4. The fitted parameters using $\sigma(E) = aE^{\gamma}$ in which $E = 0.26 - 52.51$ kJ.mol^{-1}.

R	a	γ	$\Gamma(\gamma+2)$	$k(T)$ (cm^3.molecule^{-1}.s^{-1})
1	25.9	0.40	1.24	$3.14 \times 10^{-10} \times T^{0.9}$
2	32.8	0.96	1.93	$4.7 \times 10^{-10} \times T^{1.46}$
3	3.90	0.60	1.43	$4.47 \times 10^{-10} \times T^{1.1}$
4	18.8	0.93	1.88	$6.63 \times 10^{-9} \times T^{1.43}$
5	7.80	0.48	1.30	$1.85 \times 10^{-10} \times T^{0.98}$
6	1.90	0.21	1.11	$1.49 \times 10^{-12} \times T^{0.71}$
7	1.40	0.14	1.06	$1.91 \times 10^{-11} \times T^{0.64}$
8	23.6	1.10	2.19	$1.14 \times 10^{-8} \times T^{1.6}$
9	0.60	0.29	1.16	$5.42 \times 10^{-13} \times T^{0.8}$
10	70.6	1.10	2.19	$3.40 \times 10^{-8} \times T^{1.6}$
11	18.2	0.36	1.20	$1.62 \times 10^{-11} \times T^{0.86}$
12	1.30	0.20	1.10	$3.01 \times 10^{-12} \times T^{0.7}$
13	0.90	0.30	1.17	$4.72 \times 10^{-11} \times T^{0.8}$
14	0.13	0.57	1.39	$2.01 \times 10^{-12} \times T^{1.07}$
15	2.80	0.37	1.20	$8.32 \times 10^{-12} \times T^{0.87}$
16	0.60	0.005	1.00	$1.53 \times 10^{-11} \times T^{0.5}$
17	2.30	0.28	1.15	$1.02 \times 10^{-12} \times T^{0.78}$
18	8.20	0.90	1.83	$6.96 \times 10^{-10} \times T^{1.4}$
19	2.40	0.30	1.16	$1.25 \times 10^{-10} \times T^{0.8}$
20	0.90	0.30	1.16	$4.48 \times 10^{-11} \times T^{0.8}$

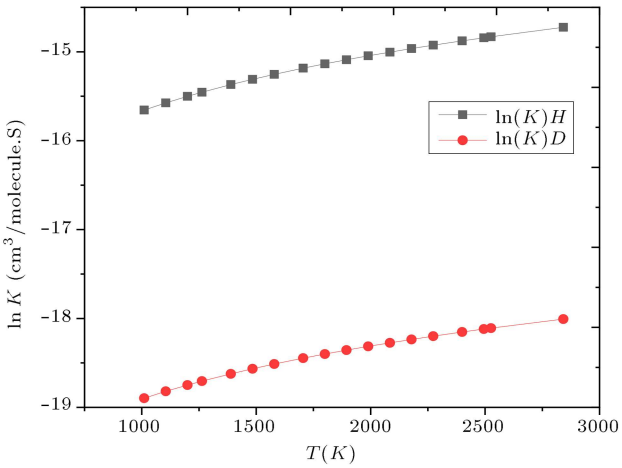

Figure 13. Arrhenius plot of the calculated rate constants drawn for $R1$ and $R11$ reactions.

classified into two types of reaction including hydrogen branch ($R1$) and deuterium branch ($R11$).

However, according to these results, it can be seen that the ratio between the rate coefficients $R1$ and $R11$ depends on the mass of the reactants.

As seen in Figure 13 and Table 4, rate constant and reaction probability for$R1$ reaction are more than $R11$reaction. Based on the rate expressions and Figure 13, the rate of hydrogen attacking reaction is greater than the deuterium attacking reaction ($R1 > R11$). The rate constant of other important trajectories is reported in Table 4. As reported in the previous paper [35] and explained elsewhere [37], given the differences in the vibrational, rotational, tunneling, and translational parameters of the reactions, when a hydrogen atom is substituted by an deuterium isotope atom, the reaction will have a different rate.

$$(k_H/k_D) = \eta_{tun} \times \eta_{rot} \times \eta_{vib} \times \eta_{trans}, \tag{12}$$

$$\eta_{rot} = \frac{Q^{TS}_{rot,H}/Q^{reactant1}_{rot,H} \times Q^{reactant2}_{rot,H}}{Q^{TS}_{rot,D}/Q^{reactant1}_{rot,D} \times Q^{reactant2}_{rot,D}}, \tag{13}$$

$$\eta_{vib} = \frac{Q^{TS}_{vib,H}/Q^{reactant1}_{vib,H} \times Q^{Treactant2}_{vib,H}}{Q^{TS}_{vib,D}/Q^{reactant1}_{vib,D} \times Q^{reactant2}_{vib,D}}, \tag{14}$$

$$\eta_{trans} = \frac{\left(m^{TS}/m^{reactant1} \times m^{reactant2}\right)^{3/2}_{H}}{\left(m^{TS}/m^{reactant1} \times m^{reactant2}\right)^{3/2}_{D}}, \tag{15}$$

where Q and m are the partition function and mass of species, respectively.

In Table 5, k_1/k_{11} is reported to determine the kinetics isotope effects. In this part, the impact of the mass of the species was determined on η_{trans} (and eventually on the rate of each reaction). Eq. (15) was used to obtain the translational section, η_{trans}, in which the mass of transition state was equal to the sum of the mass of reactants. η_{trans} value is 1.049 for ($R1 > R11$).

Table 6 reports the kinetics isotope effects on the rate constant at all trajectories in several translational energies in which k_1/k_{11}, k_2/k_{12}, k_3/k_{13}, k_4/k_{14}, k_5/k_{15}, k_6/k_{16}, k_7/k_{17}, k_8/k_{18}, k_9/k_{19}, k_{10}/k_{20} were the ratio of rate constant of reaction of hydrogen branch with the deuterium branch (CNOH/CNOD HON + C/HON + D, ONC + H/ONC + D, HOCN/DOCN, HOC + N/HOD + N, OCN + H/OCN + D, OCNH/OCND, CNH + O/CND + O and CO + NH/CO + ND).

Table 5. Primary KIE on the calculation of rate constant.

E (kJ.mol^{-1})	$\left(\frac{k_1}{k_{11}}\right)$	$\left(\frac{\sigma_1}{\sigma_{11}}\right)$	$\eta_{trans}\left(\frac{R_1}{R_{11}}\right)$
9.15	25.649	1.111	1.0486
9.98	25.738	1.186	1.0486
10.80	25.821	1.047	1.0486
13.30	26.036	1.262	1.0486
14.10	26.100	1.298	1.0486
16.63	26.270	1.266	1.0486
19.12	26.417	1.264	1.0486
20.78	26.505	1.035	1.0486
21.00	26.516	1.278	1.0486
23.63	26.642	1.182	1.0486

Table 6. Primary KIE on the calculation of reaction probability for the R_1 and R_{11} reactions subsets. P_i is the reaction probability of product i.

E (kJ.mol^{-1})	P_2/P_{12}	P_3/P_{13}	P_4/P_{14}	P_5/P_{15}	P_6/P_{16}	P_7/P_{17}	P_8/P_{18}	P_9/P_{19}	P_{10}/P_{20}
9.15	1.857	0.733	0.625	1.360	0.909	1.273	1.333	1.385	0.700
9.98	1.875	1.667	0.750	0.974	0.917	1.400	2.381	1.419	1.667
10.80	1.000	0.526	1.231	1.357	0.578	1.150	0.682	1.875	1.083
13.30	0.813	0.840	1.385	1.719	1.218	1.374	0.980	1.493	1.182
14.10	2.360	0.800	1.243	1.367	1.150	1.629	1.767	1.061	0.946
16.63	0.136	0.940	0.758	1.640	0.941	1.250	0.690	1.362	0.952
19.12	2.500	0.600	1.833	1.667	0.860	1.216	1.786	1.367	1.700
19.95	1.286	1.043	0.800	1.050	1.000	0.868	1.176	1.024	1.571
21.00	2.343	0.812	2.418	2.069	0.949	1.418	1.533	1.078	2.394
23.63	1.292	1.111	1.780	1.452	1.458	1.037	1.026	0.879	1.287

Another effect of the mass of a particle is to determine the type of products. Products in various branches were compared to the main reaction in that branch to illustrate this effect. Table 2 reports the ratio of every channel to the reaction probability of $R1$ and $R11$ in some different energies. Moreover, the mass of the particles is effective in the type of product produced. As shown earlier, the masses of heavier molecules in Reactions 13 and 16, compared to Reactions 3 and 6, respectively, increase the percentage of product production.

4. Conclusions

This study demonstrated that quantum dynamics and classical study could be convenient to study the kinetics and dynamics of the reaction. The dynamics, kinetics, and mechanism of the reaction of CN radical with OH and deuterated analogs on the interpolated ground-state potential energy surface in a wide range of temperatures or translational energies were investigated.

This surface was used to determine reaction probabilities and reaction cross-sections as a function of translation energy of fragments in various channels. OCNH and HOCN were two molecules located in potential energy surface valleys that appeared as intermediaries and had a significant reaction probability. Therefore, the total reaction probability and cross-section for all reactions were obtained and applied to calculate the rate constant and rate expression. Therefore, it was shown that the calculated rate constant was in good agreement with the reported values. The primary kinetics isotope effects also demonstrated the effects of mass of fragment on the physical observable properties such as reaction probability, rate constant, and cross-section. In non-reactive reactions, scattering angle and effective effects were investigated. In these collisions, the effects of the impact parameter and relative energy of particles on the scattering angle were demonstrated.

References

1. Sexton, K. and Adgate, J.L. "Looking at environmental justice from an environmental health perspective", *Journal of Exposure Science & Environmental Epidemiology*, **9**(1), pp. 3–8 (1999).
2. Association, A.L. "Urban air pollution and health inequities: A workshop report", *Environmental Health Perspectives*, **109**(suppl 3), pp. 357–374 (2001).
3. Herbst, E. "Chemistry in the interstellar medium", *Annual Review of Physical Chemistry*, **46**(1), pp. 27–54 (1995).
4. Hall, P. and Williams, D.A. "Polyatomic molecules in diffuse clouds", *Astrophysics and Space Science*, **229**(1), pp. 49–61 (1995).
5. Oran, E.S. "Astrophysical combustion", *Proceedings of the Combustion Institute*, **30**(2), pp. 1823–1840 (2005).
6. Sharafdini, R. and Ramazani, S. "Dynamic and kinetic parameters and energy exchanges of particles in reaction of NH+OH and deuterated analogues on an interpolated potential energy surface", *Chemistry Select.*, **5**(12), pp. 3518–3528 (2020).
7. Lique, F., Dubernet, M.l., Spielfiedel, A., et al. "Rotational excitation of sulfur monoxide in collision with helium at high temperature", *Astronomy & Astrophysics*, **450**(1), pp. 399–405 (2006).
8. Toboła, R., Dumouchel, F., Klos, J., et al. "Calculations of fine-structure resolved collisional rate coefficients for the NH($X^3\Sigma_-$)-He system", *The Journal of Chemical Physics*, **134**(2), pp. 024305–024313 (2011).
9. Warnatz, J., Maas, U., and Dibble, R.W., *Physical and Chemical Fundamentals, Modeling and Simulation, Experiments, Pollutant Formation*, Springer, Berlin, Frenklach, M, Wang, H (1990).

10. WC Jr, G., *Gas-Phase Combustion Chemistry*, Springer Science & Business Media (1999).
11. Miller, J.A. and Bowman, C. "Mechanism and modeling of nitrogen chemistry in combustion", *Prog. Energy Combust. Sci.*, **15**, pp. 287–338 (1989).
12. Cherchneff, I. and Glassgold, A.E. "The formation of carbon chain molecules in IRC+10216", *The Astrophysical Journal*, **419**, pp. 41–44 (1993).
13. Millar, T. and Herbst, E. "A new chemical model of the circumstellar envelope surrounding IRC+ 10216", *Astronomy and Astrophysics*, **288**, pp. 561–571 (1994).
14. Doty, S.D. and Leung, C.M. "Detailed chemical modeling of the circumstellar envelopes of carbon stars: Application to IRC+10216", *The Astrophysical Journal*, **502**(2), pp. 898–908 (1998).
15. Wooldridge, S.T., Hanson, R.K., and Bowman, C.T. "A shock tube study of reactions of CN with HCN, OH, and H_2 using CN and OH laser absorption", *International Journal of Chemical Kinetics*, **28**(4), pp. 245–258 (1996).
16. A′Hearn, M.F., Hoban, S., Birch, V., et al. "Cyanogen jets in comet Halley", *Nature*, **324**, pp. 649–651 (1986).
17. Liu, K. and Wagner, A.F., *The Chemical Dynamics and Kinetics of Small Radicals*, World Scientific, Singapore (1995).
18. Ruscic, B., Feller, D., Dixon, D.A., et al. "Evidence for a lower enthalpy of formation of hydroxyl radical and a lower gas-phase bond dissociation energy of water", *The Journal of Physical Chemistry A*, **105**(1), pp. 1–4 (2001).
19. Lee, T.J. and Rendell, A.P. "The structure and energetics of the HCN-HNC transition state", *Chemical Physics Letters*, **177**(6), pp. 491–497 (1991).
20. Rinnenthal, J.L. and Gericke, K.H. "Direct high-resolution determination of the singlet-triplet splitting in NH using stimulated emission pumping", *Journal of Molecular Spectroscopy*, **198**(1), pp. 115–122 (1999).
21. Zyrianov, M., Droz-Georget, Th., Sanov, A., et al. "Competitive photodissociation channels in jet-cooled HNCO: Thermochemistry and near-threshold predissociation", *The Journal of Chemical Physics*, **105**(18), pp. 8111–8116 (1996).
22. Decker, B.K. and Macdonald, R.G. "Determination of the rate constant for the tadical-radical reaction $CN(X^2\Sigma^+)$+$OH(X^2\Pi)$ at 292 K", *The Journal of Physical Chemistry A*, **107**(43), pp. 9137–9146 (2003).
23. Frisch, M., Trucks, G.W., Schlegel, H.B., et al., *Gaussian 03, Revision c. 02*; Gaussian, Inc., Wallingford, CT, **4** (2004).
24. Collins, M.A. "Molecular potential-energy surfaces for chemical reaction dynamics", *Theoretical Chemistry Accounts*, **108**(6), pp. 313–324 (2002).
25. Ischtwan, J. and Collins, M.A. "Molecular potential energy surfaces by interpolation", *The Journal of Chemical Physics*, **100**(11), pp. 8080–8088 (1994).
26. Thompson, K.C., Jordan, M.J., and Collins, M.A. "Polyatomic molecular potential energy surfaces by interpolation in local internal coordinates", *The Journal of Chemical Physics*, **108**(20), pp. 8302–8316 (1998).
27. Ramazani, S., Frankcombe, T.J., Andersson, S., et al. "The dynamics of the H_2+CO+ reaction on an interpolated potential energy surface", *J. Chem. Phys.*, **130**(24), pp. 244302–244311 (2009).
28. Bettens, R.P. and Collins, M.A. "Learning to interpolate molecular potential energy surfaces with confidence: A Bayesian approach", *The Journal of Chemical Physics*, **111**(3), pp. 816–826 (1999).
29. Jordan, M.J., Thompson, K.C., and Collins, M.A. "The utility of higher order derivatives in constructing molecular potential energy surfaces by interpolation", *The Journal of Chemical Physics*, **103**(22), pp. 9669–9675 (1995).
30. Farwig, R. "Multivariate interpolation of scattered data by moving least squares methods", in *Algorithms for Approximation*, Clarendon Press, pp. 193–211 (1987).
31. Lancaster, P. and Salkauskas, K., *Curve and Surface Fitting, An Introduction*, London, Academic Press (1986).
32. Sharafdini, R. and Ramazani, S. "Molecular potential energy surface constructed from ab initio interpolation for HCN^-+H reaction and deuterated analogues", *Molecular Physics*, **115**(7), pp. 860–868 (2017).
33. Padash, R. and Ramazani, S. "Collision processes, dynamic and kinetic parameters, and energy exchanges of particles in astrochemistry reaction of NH +H_2 and deuterated analogs on an interpolated potential energy surface", *Molecular Astrophysics*, **20**(3), pp. 1–49 (2020).
34. Dashtaki, S.L.H. and Ramazani, S. "Variational transition state theory with multidimensional tunnelling and kinetic isotope effects in the reactions of C_2H_6, C_2H_5D and C_2D6 with CCl3 to produce CHCl3 and $CDCl_3$", *Molecular Physics*, **114**(14), pp. 2195–2203 (2016).
35. Ramazani, S. "Direct-dynamics VTST study of hydrogen or deuterium abstraction and C—C bond formation or dissociation in the reactions of CH_3+CH_4, CH_3+CD_4, CH_3D+CD_3, CH_3CH_3+H, and CH_3CD_3+D", *The Journal of Chemical Physics*, **138**(19), pp. 194305–194315 (2013).
36. Kunc, J.A. "Analytical dependence of the viscosity cross sections and viscosity coefficients on parameters of intermolecular potentials", *The Journal of Chemical Physics*, **99**(6), pp. 4705–4717 (1993).
37. Zhang, L., Liu, D., Song, Y., et al. "Examining the isotope effect on CH decay and H exchange reactions: $H(^2S)$+$CH(D/T)$ $(^2\Pi)$", *Physica Scripta*, **96**(1), pp. 015404–015410 (2020).

Biographies

Afrooz Sabah received the MSc degree in Physical Chemistry from the University of Marvdasht, Fars,

Iran. She began her PhD studies at Yasouj University in 2014 under the supervision of Dr. Shapour Ramazani. Her research interests include interstellar reactions and study of the kinetic isotope effect.

Shapour Ramazani is an Associate Professor at the Chemistry Department of Yasouj University. He obtained his PhD degree from Chemistry Department of Shiraz University in 2008, followed by a one-year sabbatical period at the Australian National University (Professor Michael Collins's group). His current research interests focus on kinetics and dynamics of biology reactions and interstellar reactions and study of the kinetic isotope effect.